Atmospheric Research 202 (2018) 10–22

Contents lists available at ScienceDirect

Atmospheric Research

journal homepage: www.elsevier.com/locate/atmosres

Impact of the surface wind flow on precipitation characteristics over the southern Himalayas: GPM observations

Aoqi Zhang[a], Yunfei Fu[a,*], Yilun Chen[a], Guosheng Liu[b], Xiangdong Zhang[c]

[a] School of Earth and Space Sciences, University of Science and Technology of China, Hefei 230026, China
[b] Department of Earth Ocean & Atmospheric Science, Florida State University, Tallahassee, Florida 32306, USA
[c] International Arctic Research Center and Department of Atmospheric Sciences, University of Alaska Fairbanks, 930 Koyukuk Dr., Fairbanks, AK 99775, USA

ARTICLE INFO

Keywords:
Southern Himalayas
Precipitating systems
Surface wind
Precipitation trigger
DSD
Dual-frequency radar

ABSTRACT

The distribution and influence of precipitation over the southern Himalayas have been investigated on regional and global scales. However, previous studies have been limited by the insufficient emphasis on the precipitation triggers or the lack of droplet size distribution (DSD) data. Here, precipitating systems were identified using Global Precipitation Mission dual-frequency radar data, and then categorized into five classes according to surface flow from the European Centre for Medium-Range Weather Forecast Interim data. The surface flow is introduced to indicate the precipitation triggers, which is validated in this study. Using case and statistical analysis, we show that the precipitating systems with different surface flow had different precipitation characteristics, including spatio-temporal features, reflectivity profile, DSD, and rainfall intensity. Furthermore, the results show that the source of the surface flow influences the intensity and DSD of precipitation. The terrain exerts different impacts on the precipitating systems of five categories, leading to various distributions of precipitation characteristics over the southern Himalayas. Our results suggest that the introduction of surface flow and DSD for precipitating systems provides insight into the complex precipitation of the southern Himalayas. The different characteristics of precipitating systems may be caused by the surface flow. Therefore, future study on the orographic precipitations should take account the impact of the surface flow and its relevant dynamic mechanism.

1. Introduction

The Tibetan Plateau and the Himalayas have an important impact on the South Asian Summer Monsoon (SASM) (Benn and Owen, 1998; Yanai et al., 1992). The heating of the plateau in the summer drives the SASM into the Northern Hemisphere (Molnar et al., 1993), while the northward movement of SASM is blocked by the Tibetan Plateau and the Himalayas (Wu et al., 2012). During the SASM period, the interaction of the Tibetan Plateau and the monsoon exerts a significant impact on the weather and climate over the surrounding regions, especially the Southern Himalayas (Duan and Wu, 2005; Fu et al., 2018; Hsu and Liu, 2003). A large amount of precipitation is forced over the Southern Himalayas, making the Southern Himalayas a key area for studying the impact of the monsoon and the topography on the precipitation (Gadgil and Sajani, 1998; Jr. Houze et al., 2007). Because of the sparse ground observations and the complex terrain over the Southern Himalayas, the space-based radar is the single most effective tool in observing precipitation in this region (Bhatt and Nakamura, 2005; Romatschke et al., 2010).

Based on the observations by the Tropical Rainfall Measuring Mission (TRMM) precipitation radar (PR), there has been progress in our understanding of the rainfall response to the SASM and the topographic forcing over the Southern Himalayas. Barros et al. (2000) suggested that the mesoscale convective systems are associated with elevations of 1–2 km over the steep terrain. Bookhagen and Burbank (2006) identified two distinct rainfall maxima at elevations of 0.9 km and 2.1 km along the strike of Himalayas, which goes from the southern plain to the northern plateau. Anders et al. (2006) identified several topographic forcing factors, indicating that the surface saturation vapor pressure multiplied by the slope can represent the impact of topography on the average precipitation. Romatschke and Houze (2011) pointed out that in the afternoon more precipitating systems form at the slope than the foothills, whereas during the night more precipitating systems form over the Himalayan foothills. Qie et al. (2014) concluded that the average storm top altitudes over the Himalayas are the highest compared to the surrounding regions. Using 15 years (1998–2012) of TRMM data, Fu et al. (2018) found rain frequency increased as rain intensity decreased from the foothills to the top of the Himalayas.

---

[*] Corresponding author.
E-mail address: fyf@ustc.edu.cn (Y. Fu).

https://doi.org/10.1016/j.atmosres.2017.11.001
Received 14 July 2017; Received in revised form 12 October 2017; Accepted 2 November 2017

With the launch of the Global Precipitation Mission (GPM) Dual-frequency Precipitation Radar (DPR), the joint observation of Ku-band (13.6 GHz, KuPR) and Ka-band (35.5 GHz, KaPR) radars has provided an advanced platform for observing rainfall over the Southern Himalayas (Hou et al., 2014). KuPR is similar to TRMM PR with the same rain rate sensitivity of 0.5 mm/h and is more reliable in detecting intense precipitation (Kubota et al., 2014). On the other hand, KaPR is more sensitive to weak precipitation (rain rate sensitivity of 0.2 mm/h) than to intense precipitation due to a shorter wavelength (L'Ecuyer and Stephens, 2002). According to the different echo characteristics between Ku-band and Ka-band, dual frequency inversion algorithms are used in retrieving precipitation parameters such as the drop size distribution (DSD), storm top altitudes, and rain rate profiles (Beauchamp et al., 2015; Rose and Chandrasekar, 2006). The dual-frequency products have been validated by numerous studies (Hamada and Takayabu, 2015; Kotsuki et al., 2014). By using GPM dual-frequency data, the previous works on the rainfall over the Southern Himalayas can be further expanded.

There have also been numerous studies focusing on how the precipitations in the Southern Himalayas were triggered. Houze et al. (2007) found that the mountain-valley breeze likely played a role in the trigger mechanism. Boos and Kuang (2010) suggested that the Himalayas produce a strong monsoon by mechanically insulating continental India and the extra-tropics. Wu et al. (2007) interpreted the Tibetan Plateau as a sensible heat pump, driving local ascent that causes low-level moist air to converge. Wang et al. (2016) identified a new mechanism that precipitation occurs over the southern slopes of the Tibetan Plateau when sensible heating is suppressed. The heating mechanism that triggers the ‘tower mast’ precipitation of the Tibetan Plateau may also be responsible for precipitation over the Southern Himalayas (Fu et al., 2006). These different triggers result in various rainfall structures in the Southern Himalayas. Therefore, an environmental parameter that interacts with the precipitation mechanisms should be included in a study of Himalayan precipitation.

Such environmental parameters include the movement of the surface wind, which is crucial to the sensible heating conditions and part of the atmospheric circulation (Yang et al., 2011). It has been suggested that the directions of surface wind are influenced by the precipitation mechanisms. For example, the surface air moves upslope under the heat pump mechanism (Wu et al., 2007), while it moves downslope under the valley wind effect. Assuming mechanical insulation as the only topographical disturbance, the atmospheric flow transport to the Tibetan Plateau moves mainly around the plateau since the elevation of the Tibetan Plateau is far above the critical climbing flow height, which is around 1.5 km (Trenberth and Chen, 1988). When the local heating over the slope is the dominant control, the mean near-surface horizontal flow tends to be weaker than 1 m/s (Wang et al., 2016).

In this study, by using the advanced rainfall sensor onboard the GPM and introducing the surface wind flow to the precipitating systems, we analyzed the precipitation over the Southern Himalayas to address the following scientific questions. Is the precipitating characteristics observed by GPM DPR consistent with the previous TRMM studies over the Southern Himalayas? What is the dominant type of surface flow for precipitating systems over the Southern Himalayas? What is the distribution of precipitating systems with different types of surface flow? What is the relationship between the surface wind flow and the precipitation characteristics? Does the surface wind flow of the precipitating systems match the precipitation mechanisms?

Following this introduction, the data and categorizing method used in the study are introduced in Section 2. A sample analysis of five categories of precipitating systems is presented in Section 3.1. Then statistics were used to analyze the horizontal distributions, structural features, and relations to the terrain for five categories of precipitating systems in Section 3.2, 3.3, and 3.4, respectively. A summary and conclusions are provided in Section 4.

2. Data and method

2.1. DPR-based precipitating system dataset

The GPM DPR is the world's first space-based dual-frequency radar. Designed by the Japan Aerospace Exploration Agency (JAXA) and the National Institute of Communication Technology (NICT), DPR covers the world from 65°S to 65°N. The DPR is composed of a Ku-band Radar (KuPR, 13.6 GHz radar) and a Ka-band Radar (KaPR, 35.5 GHz radar). KuPR works in the normal scan (NS) mode with a minimum detectable reflectivity of 14.5 dBZ (Hamada and Takayabu, 2015). The KaPR works in the matched scan (MS) mode and the high-sensitivity scan (HS) mode. The relevant minimum reflectivity values for the two scan modes are 16.7 dsBZ and 10.2 dBZ (Hamada and Takayabu, 2015), respectively. The measurement accuracies of these three scan modes are all within 1 dBZ (Hou et al., 2014), and the sampling of them can be seen in Kotsuki et al. (2014).

We used the DPR_MS precipitation product at monsoon seasons (June–September) from 2014 to 2016. This precipitation product is the dual-frequency product based on the MS of KuPR and KaPR. DPR_MS has a horizontal resolution of 5 km and a nominal vertical range resolution of 250 m, sampled every 125 m. DPR_MS contains the 3D structural information from 22 km to the surface. DPR_MS provides the derived precipitation rate, type, top, and DSD. In addition, the corresponding KuPR reflectivity profiles to the DPR_MS were also used.

Based on the DPR_MS precipitation information, the precipitating system dataset was derived through an identification algorithm described in Liu and Zipser (2005), which is in heritage of the long-time TRMM era and has been widely used by both the TRMM and GPM communities (Nesbitt et al., 2000; Houze et al., 2007; Chen and Fu, 2017). The precipitating systems were defined as contiguous DPR_MS pixels with a near-surface rain rate greater than 0 mm/h. Precipitating systems with an area less than 100 km^2 contribute less than 10% precipitations in the Himalayas (Romatschke and Houze, 2011), and, as a result, only the precipitating systems with four or more pixels were considered in our statistical study.

2.2. Wind direction and study region

The Himalayan surrounding area was divided into four regions according to the topography and spatial distribution of rainfall in (Fu et al., 2018). As is shown in Fig. 1, the four regions represent the flat Gangetic Plains (FGP), the foothills of the Himalayas (FHH), the steep slopes of southern Himalayas (SSSH), and the Himalayan-Tibetan Plateau tableland (HTPT), respectively. The averaged rain rate (Fig. 1b) indicates that most of the pre-slope precipitation during the monsoon season (June–September) occurs in FHH and SSSH. These two areas were therefore selected as our study regions, collectively referred to as the Southern Himalayas.

Fig. 1c shows the distribution of the surface specific humidity for June–September 2014–2016. As a result of the elevation, The HTPT region is much drier than the other regions. The eastern FGP region is apparently more humid than the western FGP. Besides, due to the interaction of monsoon and terrain, the FHH region is also very wet (Murakami, 1987; Houze et al., 2007).

The surface wind data used in this study was derived from the European Centre for Medium-Range Weather Forecast Interim (ERA-interim) reanalysis. The ERA-interim reanalysis system is derived from the latest version of the operational ECMWF system to produce an interim reanalysis for the data-rich 1990s and 2000s (Uppala et al., 2007). The configuration and performance of ERA-interim assimilation system are presented in Dee et al. (2011). In this manuscript we used the ERA-interim near-surface wind provided at 10 m height on a 0.125° × 0.125° grid at 6-h intervals to classify precipitating systems. The classification method contains four steps as following.

Firstly, precipitating systems were identified as described in Section

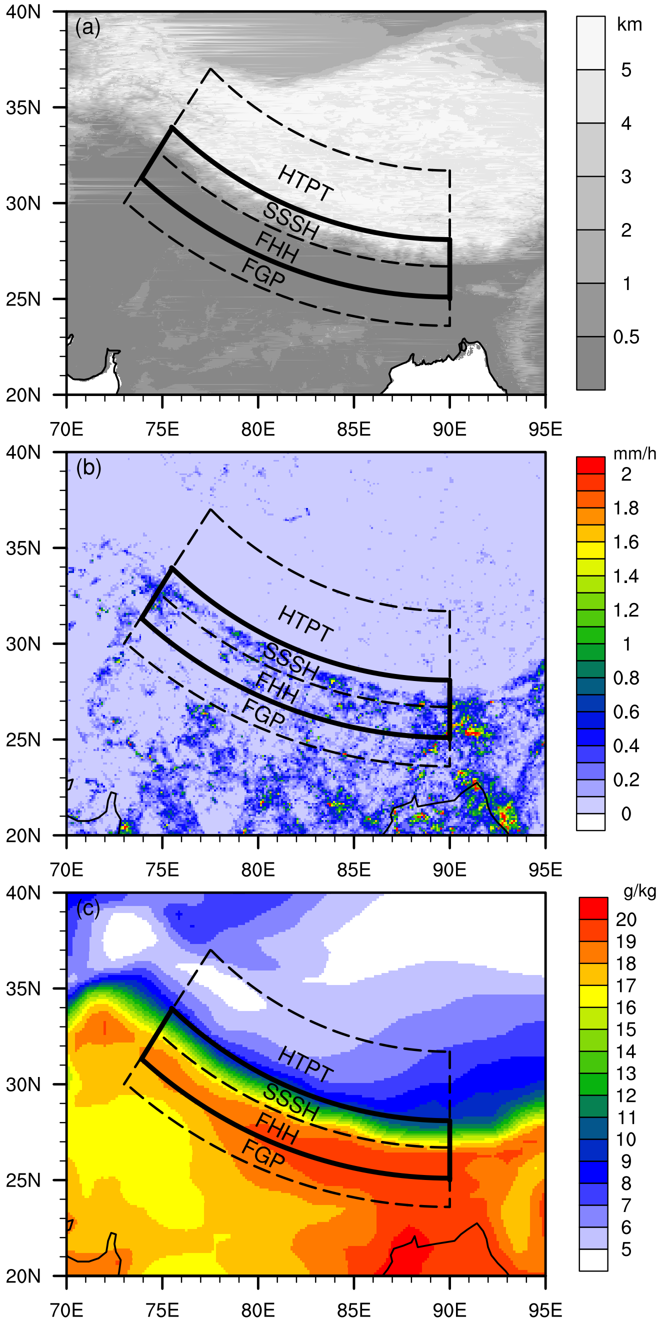

Fig. 1. The distribution of: (**a**) South Asian topography (km), (**b**) rain rate (mm/h) averaged over the study period, including non-raining periods, derived from DPR_MS for June–September 2014–2016 and (c) surface specific humidity, derived from ERA-interim for June–September 2014–2016. Our study area consists of FHH and SSSH.

2.1. Secondly, the ERA-interim 10 m wind data was matched to the DPR_MS pixels. For each DPR_MS pixel, the nearest ERA-interim grid (within ∼12.5 km and ± 3 h) was selected. Thirdly, the average winds for precipitating systems were calculated. As each precipitating system contains several DPR_MS pixels, the average wind for the precipitating system was taken as the mean wind of these DPR_MS pixels. Finally, the precipitating systems were categorized into 5 groups. The definitions of the 5 groups are also described in the following.

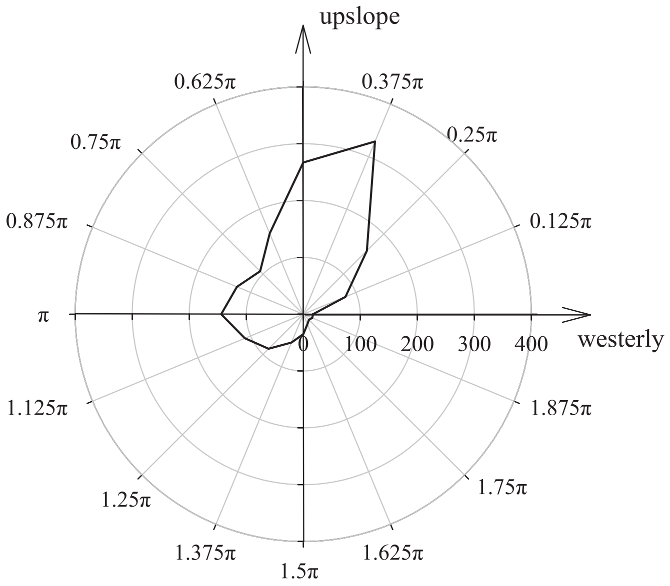

Fig. 2. The rose map of wind direction for the precipitating systems under the constructed orthogonal coordinates over the Southern Himalayas. The labels 0.125π, 0.25π, 0.375π, etc. indicate the wind direction angle. The labels 100, 200, 300, and 400 indicate the number of precipitating systems. (For interpretation of the references to color in this figure legend, the reader is referred to the web version of this article.)

Table 1
Definitions of the different precipitating system classes and the corresponding sample sizes.

Class name	Definition (r - wind speed. θ - wind direction angle)	Number of precipitating systems
I: Upslope	$r \geq 1$ m/s; $0.25\pi < \theta < 0.75\pi$	783
II: Downslope	$r \geq 1$ m/s; $1.25\pi < \theta < 1.75\pi$	95
III: Easterly circumfluent	$r \geq 1$ m/s; $0.75\pi < \theta < 1.25\pi$	390
IV: Westerly circumfluent	$r \geq 1$ m/s; $\theta > 1.75\pi$ or $\theta < 0.25\pi$	143
V: Light flow	$r < 1$ m/s	318

As shown in Fig. 1a, the concentric boundary arcs were almost parallel to the steep slopes, which was conducive to the definition of slope wind directions. As a result, the upslope direction was defined as pointing toward the concentric center and the circumfluent wind direction was defined as perpendicular to the upslope direction. These two directions formed moving orthogonal coordinates (Fig. 2), and the precipitating systems were categorized into five classes under the new coordinates (Table 1). The five precipitation classes were the upslope (I), downslope (II), easterly circumfluent (III), westerly circumfluent (IV), and light flow (V) classes. The definition and number of precipitating systems for each class are listed in Table 1. The precipitating systems of the upslope class (783) were predominant over the Southern Himalayas. The easterly circumfluent (390) and the light flow (318) classes were half the size of the upslope class. The smallest classes were the downslope (95) and westerly circumfluent (143) classes. In addition, the standard deviations of wind speeds and wind directions for five classes of precipitating systems are given in Table 2. All of the standard deviations are small, which indicates that the wind field varies little within each precipitating system.

Table 2
Standard deviations of wind speeds and wind directions for different precipitating system classes.

Class name	Standard deviation of wind speed (m/s)	Standard deviation of wind direction
I: Upslope	0.111	0.02π
II: Downslope	0.118	0.059π
III: Easterly circumfluent	0.132	0.023π
IV: Westerly circumfluent	0.085	0.02π
V: Light flow	0.106	0.112π

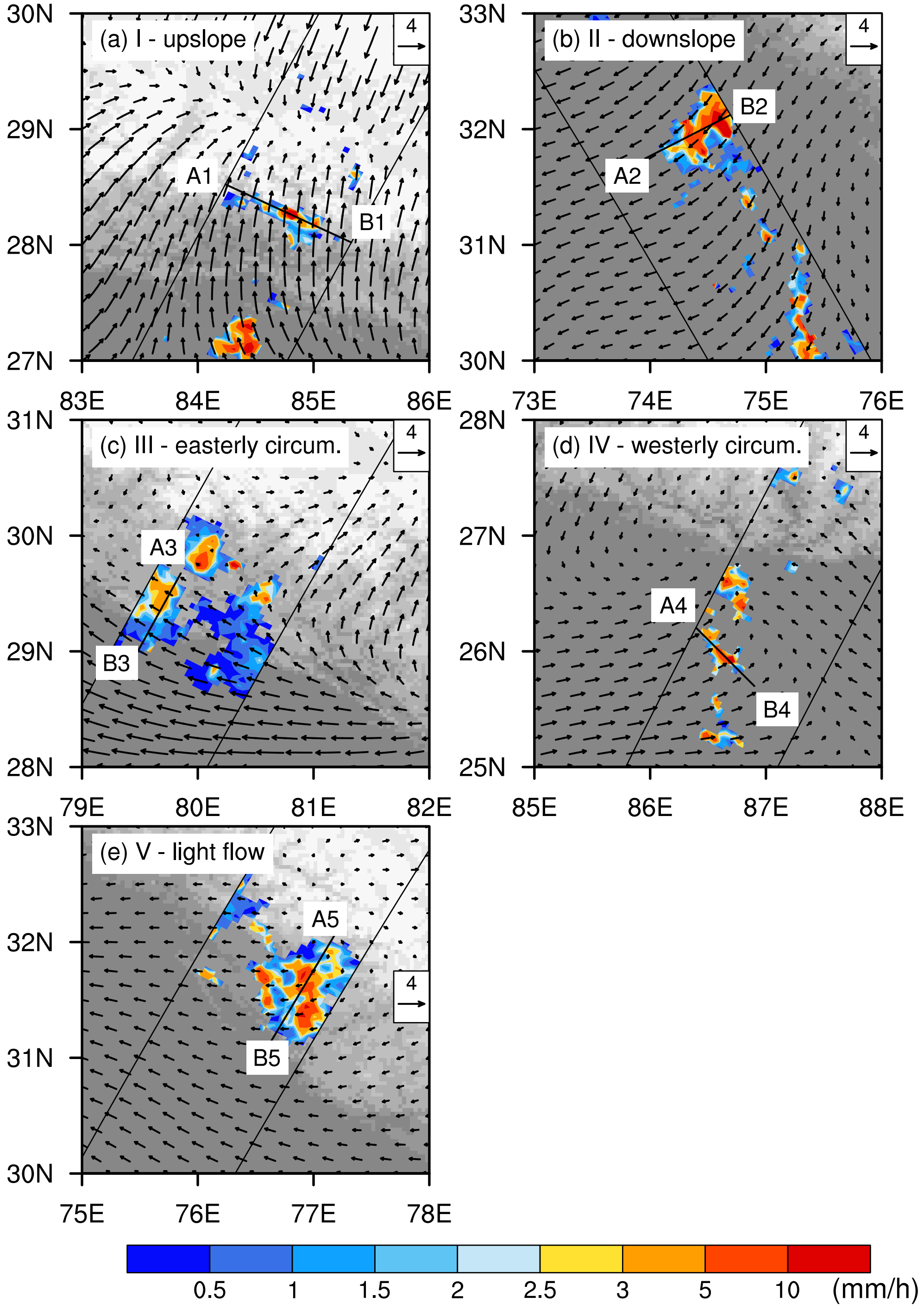

Fig. 3. Demonstration of the horizontal patterns for the different classes of Himalayan precipitating systems: (a) upslope (I); (b) downslope (II); (c) easterly circumfluent (III); (d) westerly circumfluent (IV); and (e) light flow (V) classes. The color scale indicates near-surface rain rate in mm/h. The gray scale indicates elevation and is the same to Fig. 1a. The overlapped arrows indicate the ERA-interim 10 m wind. The diagonal lines represent the edges of the DPR_MS swaths.

3. Results

3.1. Sample analysis

The introduction of the categorizing method into precipitating systems over the Southern Himalayas was new. To validate the effectiveness of the new method, we firstly studied five precipitating system case studies for each class, providing a detailed insight into the precipitation structures. Furthermore, the precipitation characteristics identified by the case studies provide a good foundation for further statistical study.

Fig. 3 shows the DPR_MS near-surface rain rates and the ERA-interim 10 m winds associated with the five precipitating systems in each category. The precipitating system in class I (Fig. 3a) was located at 2–4 km elevations on the Himalayan slopes at 0930 UTC (1500 LST) 15 July 2015. Dominated by a strong upslope surface wind, the precipitation belt was fairly narrow and highly parallel to the terrain with weak precipitation. The precipitation case of class II (Fig. 3b) occurred on the plain at 2030 UTC (0130 LST) 11 July 2015, at a specific distance ~150 km from the hills. The surrounding surface winds were moderate downslope winds with little horizontal wind shear. Within the moderate rain area, rain intensity decreased from north to south. Class III (Fig. 3c) was located at the foothills of the SSSH at 2300 UTC (0430 LST) 13 July 2016. Strong easterly circumfluent flows controlled the southern plain, but decreased rapidly within the large precipitation area. The precipitation intensity was greater over the slopes than the

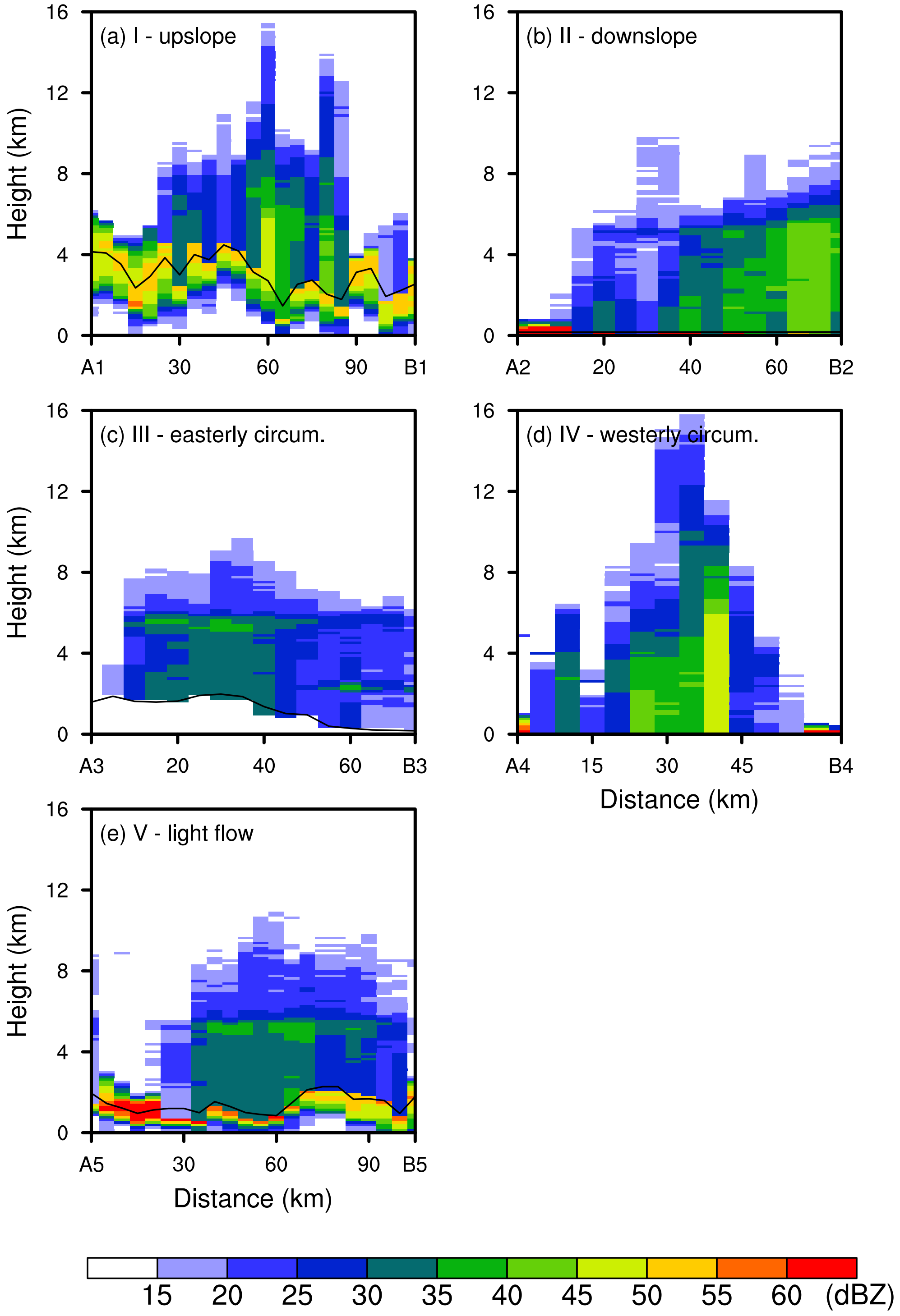

Fig. 4. Vertical cross-section of the Ku-band attenuation corrected reflectivity running left to right along the AB line in Fig. 3. The blackline in the cross-section plot indicates the height of the subtending terrain. The color scale indicates reflectivity in dBZ. The lowest measured value was ~15 dBZ.

adjacent plain. Class IV (Fig. 3d) was a specific case that occurred on the plain near the slopes at 2130 UTC (0330 LST) 24 August 2015. The westerly and easterly circumfluent low-level monsoon tributaries meet in this region, causing low-level convergence. The precipitation area was very small with dispersed intense precipitation. Fig. 3e shows the precipitation case for class V over the lower slopes at 0230 UTC (0730 LST) 10 August 2015. The surface winds were weak within concentrated precipitation area. The center of the precipitating system reached a near-surface rain rate of ~10 mm/h.

The vertical cross-sections of the Ku-band reflectivity running left to right along the AB lines in Fig. 3 are shown in Fig. 4. The highest echo top of the upslope case (Fig. 4a) exceeded 14 km, indicating a location of penetrative convection cloud (Xian and Fu, 2015; Chen and Fu, 2018), although reflectivity decreased abruptly in the adjacent pixels. The echoes of the downslope case (Fig. 4b) were within 8 km of the surface and gently changed between adjacent DPR_MS pixels. Fig. 4c confirms that the echo top altitudes and the reflectivity increased significantly over the slope for the easterly circumfluent case. In addition, the bright band is clearly visible, suggesting stratiform rainfall (Biggerstaff and Listemaa, 2000). The cross-section of the westerly circumfluent case (Fig. 4d) shows another penetrative convection with the highest echo top exceeding 16 km. Together with the upslope case, this suggests that the Southern Himalayas is a suitable place for studying penetrative convection. For the light flow case (Fig. 4e),

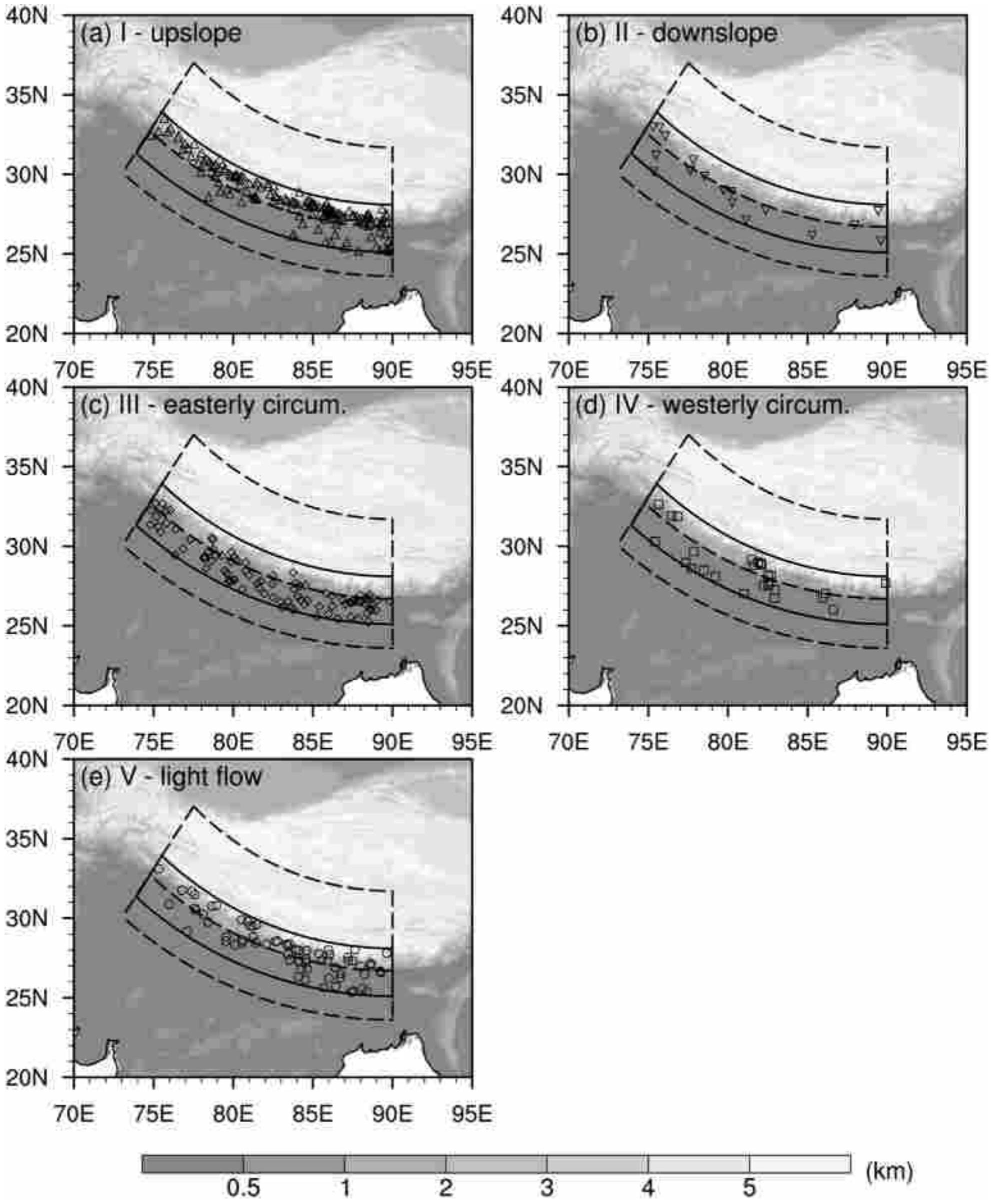

Fig. 5. Regional distribution of the large precipitating systems (> 600 km^2 in area) of (a) upslope (I); (b) downslope (II); (c) easterly circumfluent (III); (d) westerly circumfluent (IV); and (e) light flow (V) classes.

apparent bright bands occurred over the lower slopes with corresponding storm top altitudes of ~10 km. The topography of the subtending terrain (shown in black at the bottom of Fig. 4a and e) indicates that the surface echoes were not well removed over the high-relief slopes. Therefore, an elevation limit was needed for the reflectivity profile.

3.2. *Location, time, and surrounding surface movement*

The above case studies provide some indication of the characteristics of the precipitating systems over the Southern Himalayas. These will now be statistically validated and analyzed in detail in Sections 3.2–3.4. This section presents the analysis of the locations, time, and the relative surface winds.

Fig. 5 shows the locations of the large precipitating systems (> 600 km^2 in area) in each of the five classes. Similar to Table 1, most of the large precipitating systems were located in classes I, III, and V, while only a few large systems occurred in classes II and IV. The class I had most of the large precipitating systems (Fig. 5a). They occurred over all of the SSSH and the eastern FHH. However, the large precipitating systems of class I were most frequent in the eastern SSSH, downstream of the monsoon tributary from the Bay of Bengal (BOB) (Pang et al., 2012).

Conversely, the distribution of large precipitating systems in class III was fairly uniform from the eastern to the western FHH. This suggests that the moist low-level air from the BOB was consequently condensed into rain over the western foothills. The large precipitating systems of class V occurred frequently over the middle and eastern parts of the lower SSSH, where moisture had accumulated from previous interactions of the monsoon and the terrain (Fu et al., 2018).

The wind field, which reflects the source of the water vapor, is an important part of the study of precipitation in South Asia (Rasmussen and Houze, 2012; Romatschke and Houze, 2011; Wu et al., 2007). However, in previous statistical studies, the average circulation field has been simply calculated as the average of the whole region during precipitation time, which takes into account many non-precipitating regions. To reduce the impact of the non-precipitating regions, the ERA-interim wind data were required to be within 200 km and ± 3 h of the precipitating systems to limit the precipitating-relevant regions in this study. Furthermore, all subsequent statistics were based on the DPR_MS samples of all precipitating systems (> 4 DPR_MS pixels in size) in Table 1.

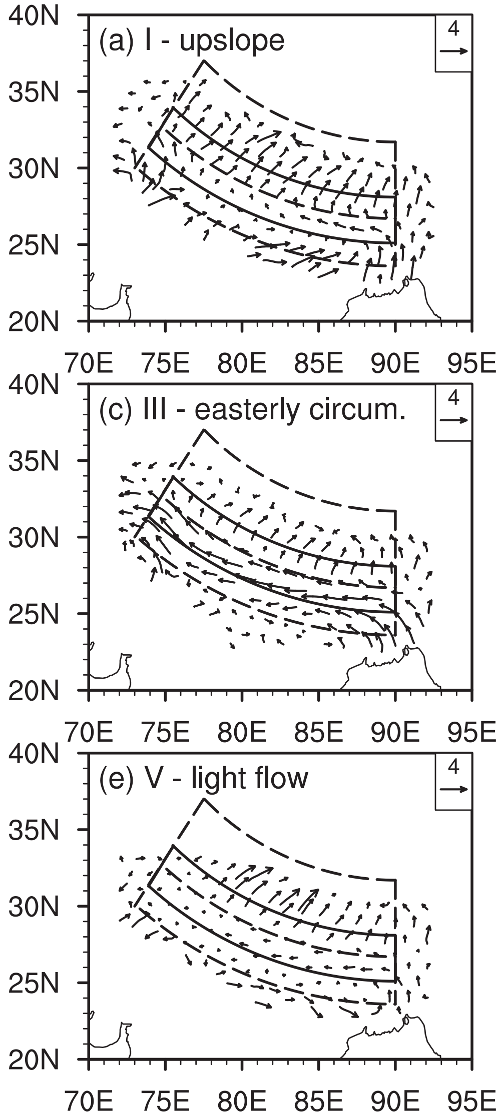

Fig. 6. Horizontal distribution of the composited surface wind for precipitating systems of: (a) upslope (I); (b) downslope (II); (c) east circumfluent (III); (d) west circumfluent (IV); and (e) light flow (V) classes. All precipitating systems with four or more DPR_MS pixels were analyzed. Only ERA-interim grids within 2° of the precipitating systems were used.

For the surface wind field of the upslope class (Fig. 6a), the southwesterly monsoon flow dominated most of the FGP region, except for the FGP region near the BOB where the wind directions were southerly. In the FHH area, the surface wind was a weak easterly circumfluent wind, measuring almost 0 m/s in the western FHH. For the SSSH and the HTPT, the surface flow demonstrated strong upslope movement, showing consistency with the locations of most of the large precipitating systems (Fig. 5a). In general, the surface circulation of the upslope class could bring warm and moist airflow to the SSSH and Tibetan Plateau. Together with the heating upstream over the Tibetan Plateau, this surface circulation represented the heat pump effect (Wu et al., 2007).

For the surface wind field of the downslope class (Fig. 6b), the FGP region was still controlled by the upslope flow. However the wind speed associated with the downslope case is much smaller than the upslope class. Weak downslope flows occurred in the SSSH area, where was accompanied by a small part of the large downslope systems (Fig. 5b). Over the FHH region, the downslope wind was relatively strong and was joined by the easterly monsoon flow, increasing the number of downslope systems here. In the FGP region, the surface wind was still generally controlled by the downslope flow with a weak convergence at approximately 85E, which can cause rising air. This result was consistent with the precipitation model in (Houze et al., 2007), who suggested that the upstream lifting, and the diurnal heating and cooling likely played a role in triggering precipitation over the central Himalayas.

The surface winds of the two circumfluent classes (Fig. 6c and d) showed great similarities. Both the SSSH and the HTPT were controlled by weak upslope winds, while the FGP and the FHH were dominated by circumfluent winds. However, the easterly circumfluent wind (Fig. 6c) originated from the BOB, transporting enough moisture and being strong enough to reach the western side of the FHH. As a result, the precipitating systems of class III accounted for a larger proportion over the Southern Himalayas. Conversely, the westerly circumfluent flow (Fig. 6d) was the monsoon tributary flowing across the arid desert, which barely reached the eastern FHH, leading to a small number of precipitating systems. These two types of circumfluent surface winds represented the two monsoon tributaries of South Asia moving around the Himalayas, and the insulation of the Himalayas may therefore have been the main terrain effect here (Boos and Kuang, 2010).

Unlike the above four types of precipitating systems, the surface wind speeds of the light flow class (Fig. 6e) were close to zero in most of the Southern Himalayas, indicating that the precipitation was less affected by other regions and thus the locally thermal changes were more important to the light flow events.

The diurnal cycles were analyzed to validate the timing consistency between the surface movements and the precipitation triggers. The precipitation time that came with the 2ADPR precipitation product is

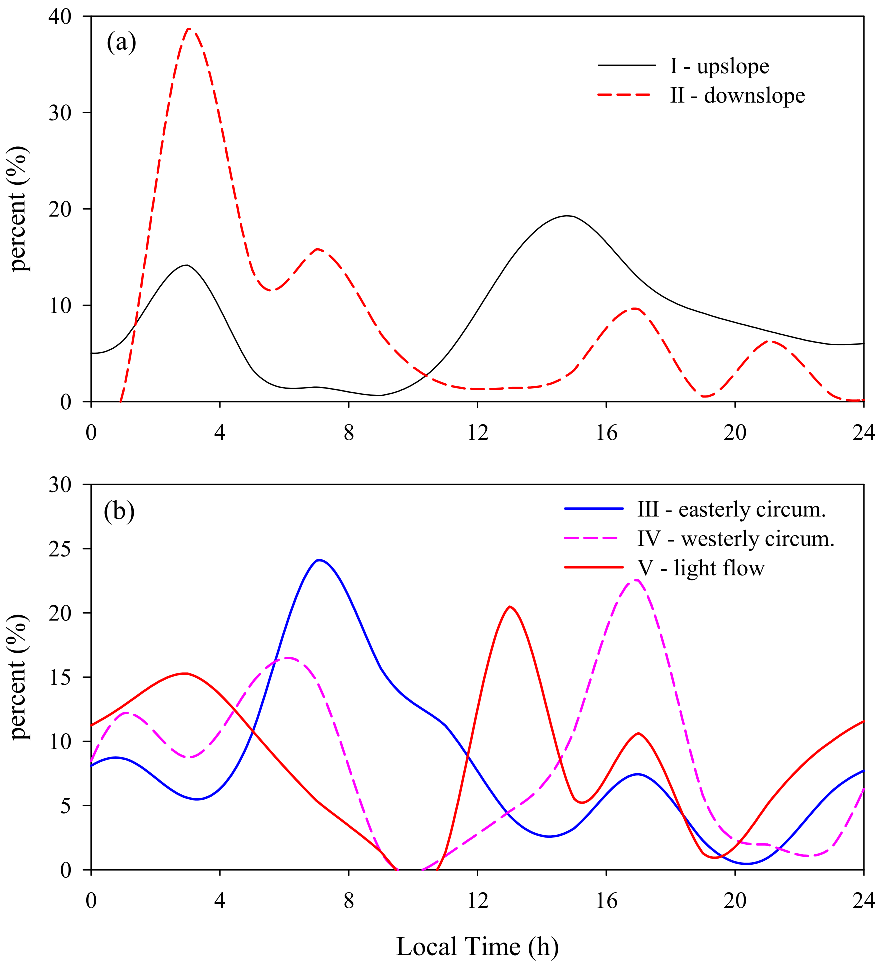

Fig. 7. Diurnal cycles of the precipitating systems for: (a) upslope (I) and downslope (II) classes; and (b) easterly circumfluent (III), westerly circumfluent (IV), and light flow (V) classes.

used here. In Fig. 7, the number of precipitating systems is listed at 3 h intervals. For class I, most precipitating systems occurred in the afternoon. At that time, the sensible heating on the Tibetan Plateau was much higher than those on its southern plain, causing the low-level air to converge toward and rise over the Tibetan Plateau (Wu et al., 2007). Conversely, the peak for class II occurred during the night, when the valley wind was the strongest during the day. For the circumfluent classes (III and IV), the precipitating systems had peak occurrences in the morning and the evening, when the sensible heat forcing was suppressed. The south and southwest monsoons tended to move around the Himalayas due to the high terrain (Trenberth and Chen, 1988). In the diurnal cycle of class V, however, peaks occurred at noon and midnight. On the one hand, the surface sensible heating was the strongest at noon during a day, so the low-level air was heated to ascend, which promote the formation of precipitation systems. On the other hand, the surface sensible heating was the most suppressed at midnight. As described in Wang et al. (2016), the air temperature and saturation specific humidity decreased, thus precipitation systems were generated from phase change. Collectively precipitating systems of class V were highly related to the surface sensible heating (either intense or suppressed).

3.3. Precipitation features

The precipitation features over the Southern Himalayas have been described by numerous previous studies (Qie et al., 2014; Shrestha et al., 2012). Our analysis focused on the classified precipitation systems, which are based on the surface wind direction. Fig. 8 displays the probability distribution function (PDF) of the three corresponding parameters (i.e., wind speed, rain rate, and storm top altitude), calculated in each pixel of the precipitating systems, to quantify the characteristic differences of the classified precipitation types.

In terms of surface wind speeds (Fig. 8a), the speed of class I reached a peak at 2 m/s. It was concentrated in the range of 0–4 m/s, which is much smaller than the surface wind speeds of the monsoon tributary, reflecting the fact that the upslope wind was highly limited by the terrain. The peak wind speed for class II was approximately 1.8 m/s with rapidly decreasing probabilities above the peak. As a result, only 10% of the wind speeds exceeded 2.5 m/s, showing consistency with the nighttime valley winds over the Southern Himalayas. The peak speed of class III was about 2.2 m/s with a wide range from 0 to 8 m/s. The PDF of the wind speeds for class IV formed an interesting double-peak structure, occurring at 1.6 and 2.4 m/s. Limited by the classification method, the wind speeds for class V were generally no more than 2 m/s.

The PDF of the near-surface rain rates (Fig. 8b) was much simpler than that of the wind speeds. The near-surface rain rates of all classes peaked in the 0.8–1 mm/h range. The total fractions of precipitation with near-surface rain rates greater than 5 mm/h (intense rainfall) were 11.8%, 7.9%, 18.4%, 9.2%, and 13.7% for the precipitating systems of class I, II, III, IV, and V, respectively. These numbers indicate a positive correlation with the moisture of surface airflow. The airflow of the easterly circumfluent class (III) originated from the BOB, carrying largest amounts of moisture, and resulted in the largest proportion of intense rainfall. The upslope (I) and light flow (V) classes, which either received sufficient moisture from the moist FGP transported by the low-level flow or had accumulated enough moisture previously, also held large amounts of intense rainfall. The surface wind of the westerly

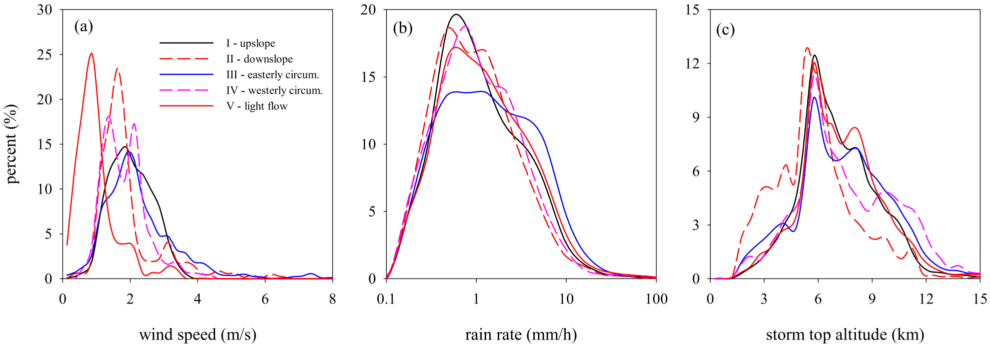

Fig. 8. PDF of (a) wind speed, (b) near-surface rain rate, and (c) storm top altitudes for the precipitation in the different classes.

circumfluent (IV) and downslope classes originated from the arid desert and Tibet, respectively, and were both accompanied by less water, resulting in small fractions of large near-surface rain rate.

Fig. 8c shows the PDF of the storm top altitudes (mean sea level height) in the Southern Himalayas. For each class, the distribution range of storm top altitudes was 1–15 km with a peak at ~6 km. Furthermore, the average height was approximately 7–8 km, which is consistent with Chen et al. (2016). The total percentages of precipitation with storm top altitudes greater than 10 km (high storm top altitudes) were 9.7%, 6.5%, 15.9%, 21.7%, and 11.3% for precipitating systems of classes I, II, III, IV, and V, respectively. This range of ratios shows consistency with that of the proportions of the intense rainfalls, except for that of class IV. Class IV had a large amount of high storm top altitudes and a small amount of intense precipitation. This suggests that much of the tallest storms were contained in class IV.

The vertical structural characteristics of precipitation can be effectively displayed by the Contoured Frequency by Altitude Diagram (CFAD) method (Yuter and Houze, 1995). Fig. 9 is the CFADs of the GPM 2ADPR Ku-band reflectivity data for June–September 2014–2016. Similar to Houze et al. (2007), the structural differences among the five classes of precipitating systems were characterized by three distinct regimes. The regimes included those located above, at, and below the 0 °C level, which was at ~5.5–6 km altitude.

Above the 0 °C level, in the ice region, the reflectivity of class II was rare, indicating that the storm top altitudes of class II were low with few large solid particles in the hydrometeor profile. Conversely, the other four types of precipitating systems had clear echo signals. At 8 km altitude, the median reflectivity values were ~18, 18, 20, and 22 dBZ for classes I, V, III, and IV, respectively.

At the 0 °C level, the tendency for a melting-layer bright band to occur in the echoes was demonstrated by a distinct rightward shift in the CFAD contours toward higher dBZ at ~5.5–6 km and another weaker leftward shift in the CFAD contours toward smaller dBZ at ~5.5 km. This corresponded to the melting process (partially melted ice particles produce the strongest echo reflectivity) of ice particles at the 0 °C level (MASON, 1972). In particular, because there were few ice echoes over the 0 °C level, the bright band of class II was very weak. Besides, the bright band of class IV was also weak, consistent with large proportion of convective precipitations in class IV events.

Below the 0 °C level in the liquid region, precipitating particles fell to the ground through collision growth and spontaneous crushing (Hocking, 1959). There was a positive correlation between the reflectivity in this region and near-surface rain rates, shown by the fact that the reflectivity of classes II and IV was clearly weaker than that of the other classes in the liquid region. In addition, significant differences existed between the CFAD contours of classes III and IV, although both are circumfluent classes. Class IV had more intense reflectivity in the ice region, but much weaker reflectivity in the liquid region, which was likely related to the humidity of the surface flow. Therefore, the DSDs of the precipitating systems of each class will be further analyzed to validate the respective precipitating processes.

3.4. *Impact of topography*

The impact of the topography on the precipitation has been studied in depth over the Southern Himalayas (Fu et al., 2018; Qie et al., 2014). Specifically, two distinct rainfall frequency peaks have been observed in the topology at ~0.6 and 2.1 km (Bookhagen and Burbank, 2006; Shrestha et al., 2012). In our study, the impacts of topology on the five classes of precipitating systems were studied based on our classification method.

Fig. 10 shows the normalized precipitating frequency in the radial cross-section (perpendicular to topography) of the study regions. Because we only accounted for precipitating systems with centers located in the FHH and SSSH regions, most DPR_MS precipitation samples were present in these two regions. This figure verifies our hypothesis for the triggering of the five types of precipitating systems. The precipitation of class I were forced by the heat pump effect, which was why the precipitation occurred mainly in the moderate SSSH region (Fig. 10a). Class II was forced by the valley wind and, corresponding to that, the samples were fairly uniform along the cross-section of the Southern Himalayas (Fig. 10b). Triggered by the isolation of the Himalayas, the sampling peaks of classes III and IV occurred at the boundary of FHH and SSSH (Fig. 10c and d). Furthermore, due to the lack of low-level moisture, many class IV samples also occurred on the moderate SSSH. The precipitating systems of class V are thought to have been produced by the surface sensible heating (either intense or depressed) (Fu et al., 2006; Wang et al., 2016). The Himalayas are located north of the Tropic of Cancer, so the sensible heating of the SSSH region is higher than the FFH region during the daytime; during the nighttime, since the slope loses heat faster than the plain, the sensible heating of the SSSH region is more depressed than the FFH region. Therefore, the DPR_MS pixels were distributed uniformly over the SSSH region for class V.

In addition to the precipitation frequency, the terrain also exerts an important effect on the near-surface rain rates, storm top altitudes, and DSDs (Qie et al., 2014; Zwiebel et al., 2016). Fig. 11 shows the near-surface rain rates, storm top altitudes, and DSDs in colored lines for the different classes of precipitating systems in the radial cross-section, similar to Fig. 10.

In the cross-section of the near-surface rain rates (Fig. 11a), the rain rates of classes II and IV were clearly much smaller than those of the other classes, which validate the conclusion that there was less water vapor in the air column for classes II and IV due to the dryer low level air relative to the other classes. The near-surface rain rates of class I reached their peak of ~4 mm/h at ~50 km distance from the foothills, and rapidly decreased in the SSSH region reaching ~2 mm/h at the mountainside. For class III, the near-surface rain rate variability was indistinct on the SSSH with a value of ~2.5 mm/h, although the values were slightly smaller than those in the FHH region (3–3.5 mm/h). The difference between the near-surface rain rates of classes I and III reflects the fact that the upslope airflow lost water vapor quickly, while the circumfluent airflow did not. The near-surface rain rates of class V were higher (3 mm/h) over the foothills and on the lower slopes, which

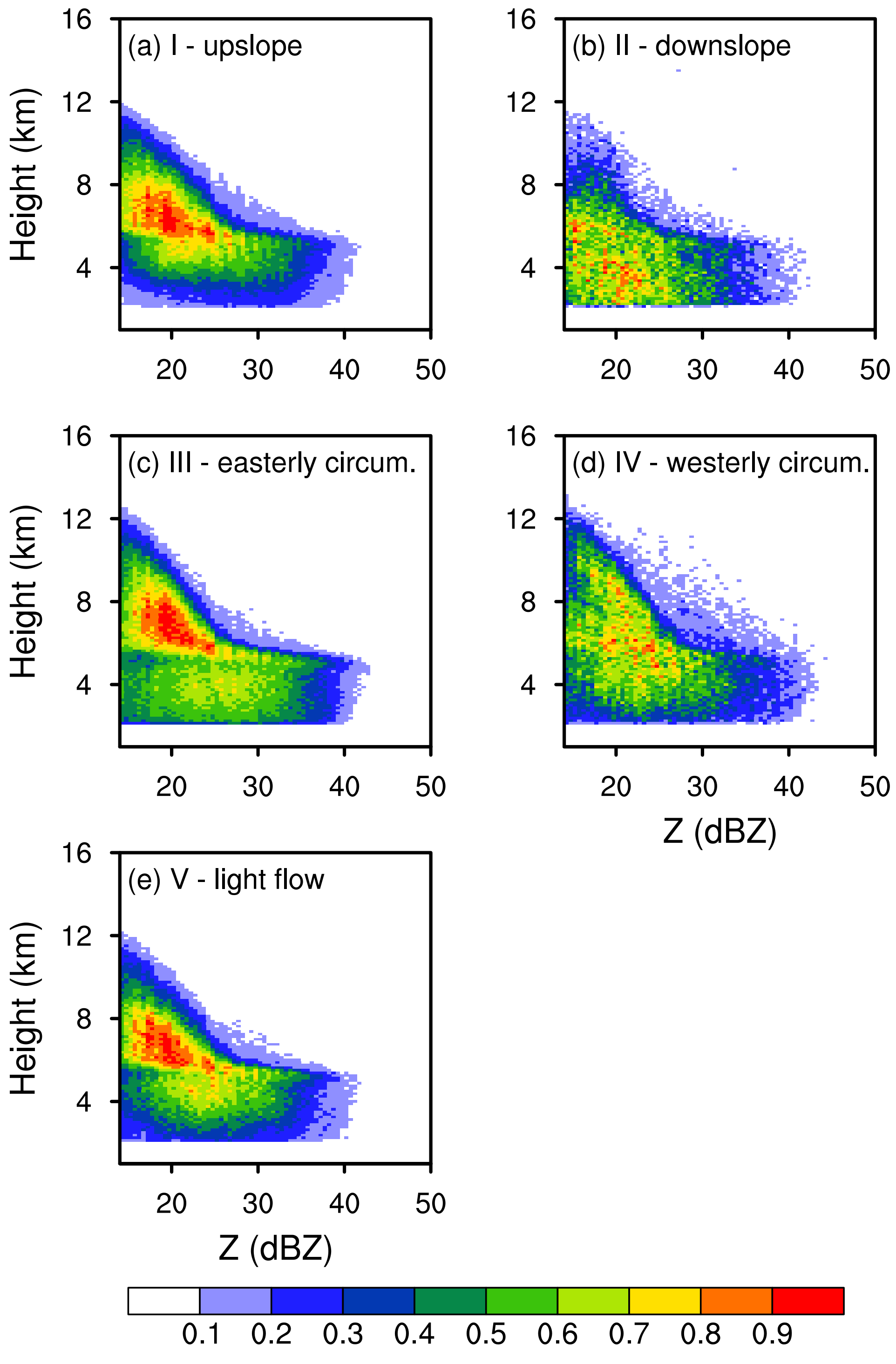

Fig. 9. CFAD of the Ku-band reflectivity data for June–September 2014–2016 for: (a) upslope (I); (b) downslope (II); (c) easterly circumfluent (III); (d) westerly circumfluent (IV); and (e) light flow (V) classes.

collect large amounts of water vapor due to latent heat fluxes off the surface (Fu et al., 2018).

The colored line of the storm top altitude (Fig. 11b) for class I, the most common class in the Southern Himalayas, shows a low value at 2 km altitude. This low value of storm top altitude is consistent with Chen et al. (2017), which suggested that the loss of water content causes the decrease of cloud top altitude. The storm top altitude for class II was less than 6.5 km over the cross-section, indicating that the ascending air was suppressed by the downslope surface wind. For precipitating systems of class III, the SSSH played a role in the slight uplift of the storm top altitude, which is also shown in Fig. 3c. The storm top altitudes of class IV reached an average of 8 km, showing the frequent occurrence of strong convection. The average storm top altitude of class V was ~7 km with an insignificant response to the terrain.

To validate the above results and to understand the micro-physical structure of the precipitating systems in the Southern Himalayas, the cross-sections of the near-surface droplet concentration and effective radius (both are DSD parameters) are shown in Fig. 11c and d. As the elevation increased, the near-surface droplet concentration and effective radius of class I decreased, showing that water content was continually lost during the climbing of the low-level airflow. The near-surface droplet concentration and effective radius of class II were consistently less than those of class I, indicating that the atmospheric water column was less in precipitating systems of class II.

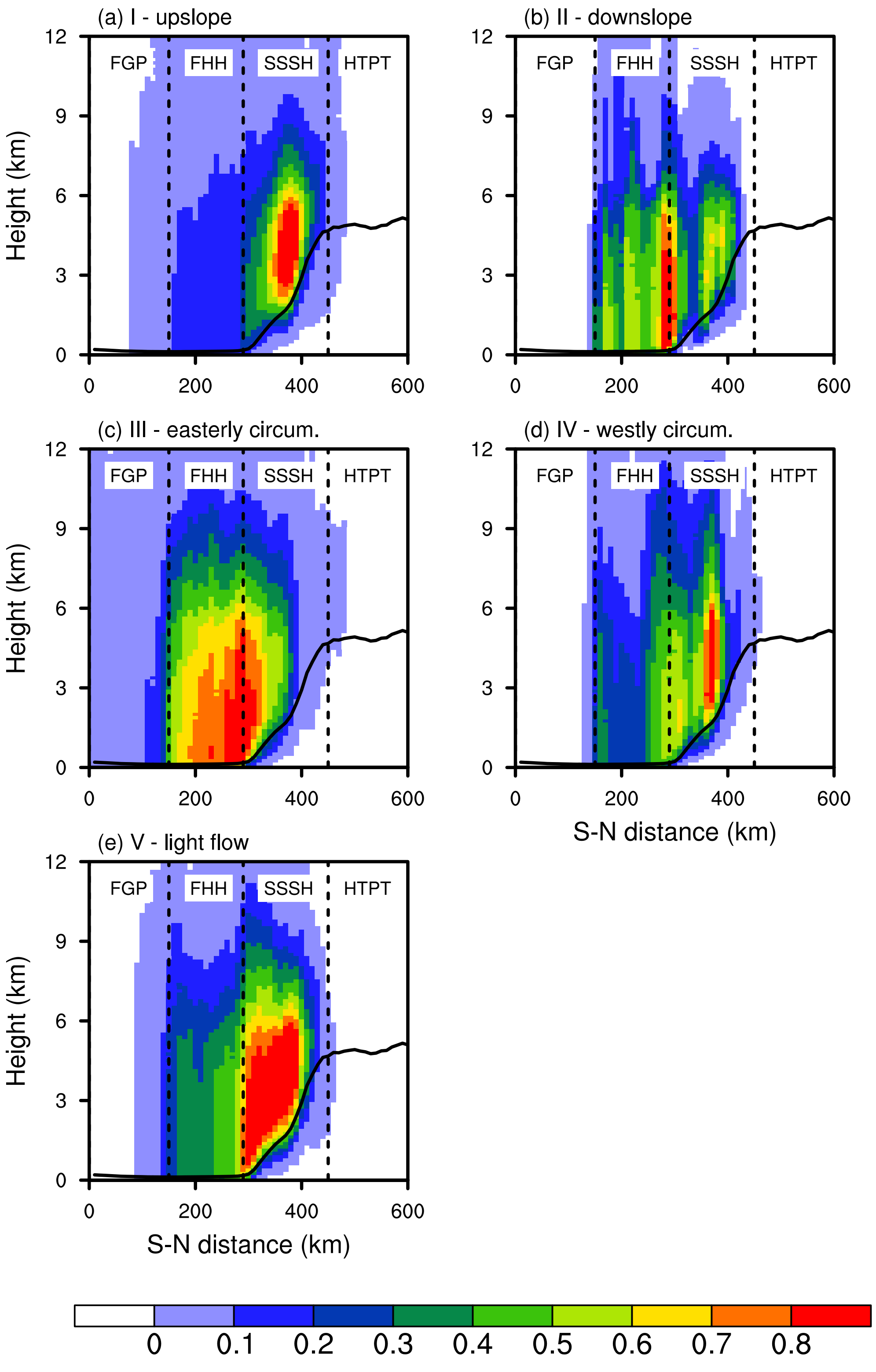

Fig. 10. Distributions of normalized precipitating frequency in each grid (0.125 km in height and 10 km along the horizontal) of the radial cross-section (perpendicular to topography) of the study regions for the precipitating systems of: (a) upslope (I); (b) downslope (II); (c) easterly circumfluent (III); (d) westerly circumfluent (IV); and (e) light flow (V) classes. The precipitating frequencies are normalized by the maximum precipitating frequency of each class.

As elevation increased for class III, the near-surface droplet concentration increased, while the effective radius decreased, which was also shown in the case study of Zwiebel et al. (2016). This suggests that the mountain weakened the collision growth in the liquid region by reducing the distance from 0 °C level to the surface, but the water content in class III keeps the same as elevation increases.

The precipitation structure of class IV was the most unique with high radar reflectivity in the ice layer, but low radar reflectivity in the liquid layer (Fig. 9d). We suggest that the low-level air of class IV was dry from the arid desert (Fig. 6d), hence more intense upward motion is needed for precipitation formation in comparison to class III event. Under this mechanism, the storm top altitude was forced high by the upward motion (Fig. 11b). However, when ice particles fell to the lower dry layer, the small particles were evaporated leading to weak near-surface rain rate (Fig. 11a). This suggestion was supported by the evidence that the near-surface droplet concentration was low while the near-surface effective radius was large (Fig. 11c–d).

Furthermore, in the FHH region, the near-surface effective radius of

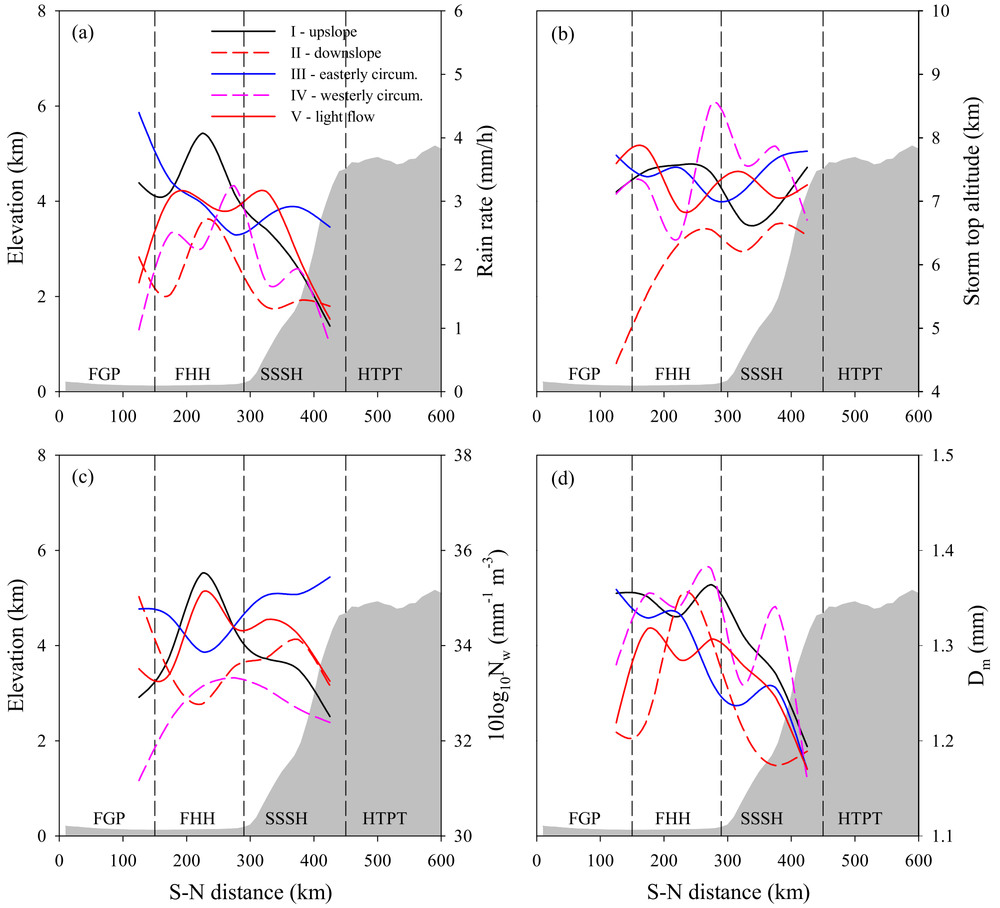

Fig. 11. Radial mean distributions of: (a) near-surface rain rates, (b) storm top altitudes, (c) near-surface droplet concentration, and (d) near-surface droplet effective radius in the radial cross-sections of the study regions. The dashed lines are the boundaries of the FGP, FHH, SHHH, and HPTP, from left to right, respectively.

class V was apparently smaller than class I events while the droplet concentration keeps the same, causing the average near-surface rain rate for class I events larger than the class V events.

4. Conclusions

To better understand the precipitation process in the Southern Himalayas, the precipitating systems were identified based on the DPR_MS precipitation data, and categorized into five classes according to surface flow from ERA-interim reanalysis data. The horizontal distributions, structural features, and relations to the terrain were investigated using case studies and statistics. The trigger mechanisms were also discussed and validated. Our results suggest that the different characteristics of precipitating systems may be caused by the surface flow. The main conclusions are:

1. The precipitating systems of the upslope class (I) were triggered by the heat pump effect. They occurred mostly in the afternoon at a moderate SSSH with a strong upslope low-level layer. The amount of atmospheric water vapor decreased when the flow climb over the SSSH, causing the near-surface droplet concentration, near-surface droplet effective radius, and near-surface rain rate to decrease over the region. Along the radial cross section of the Himalayas (perpendicular to topography), the storm top altitudes reached a minimum at the 2 km elevation of the SSSH region.
2. The precipitating systems of the downslope class (II) were forced by the valley wind during the night. They were distributed uniformly over the Southern Himalayas accompanied by weak winds from the Tibetan Plateau, which had low water content. Therefore, the precipitating systems had low near-surface droplet concentrations, small near-surface effective droplet radiuses, weak near-surface rain rates, and low rain top altitudes.
3. The precipitating systems of the easterly circumfluent class (III) were triggered by the mechanical insulation of the Himalayas. They occurred mostly at the boundary of FHH and SSSH in the morning. The low-level layer originated from the BOB with abundant moisture, and precipitation was therefore often accompanied by intense near-surface rain rates and high storm top altitudes. When the class III precipitating systems reached the slopes, collision growth in the liquid region of precipitation was constrained by the high elevation. As a result, the near-surface droplets were smaller but at a higher concentration. In addition, the storm top altitudes of class III were slightly uplifted by the terrain.
4. The precipitating systems of the westerly circumfluent class (IV) were also triggered by mechanical insulation. However, the low-level air of class IV originated from the arid desert with lower water content. There was larger proportion of convective precipitation in class IV events compared with other classes. Therefore, the echo reflectivity was high in the upper layer, whereas the echo reflectivity was small below the 0 °C layer. Due to the dry low-level layer, the small particles evaporated in this layer leading to weaker near-surface rain rates.
5. The precipitating systems of the light flow class (V) were thought to be forced by the surface sensible heating, either intense or depressed. Influenced by the precipitating mechanism, class V was common over the SSSH at noon and midnight. The storm top altitudes of light flow class were high while the near-surface precipitation particles were relatively small.

Some of the uncertainties and limitations of this study include the following. Because the precipitation types have influence on the performance of DPR rainfall algorithm, the comparisons between different categories of precipitating systems could be influenced. In addition, 3 monsoon seasons were presented in this study, which equate to about 150 total overpasses of the same location during those times. The sample size is enough for statistical study but may also exert some limitations. Future use of long-time data and consideration of the precipitation types will reduce the bias of rainfall parameters, which will be done in our further work.

Acknowledgments

This work is supported by the Third Tibetan Plateau Scientific Experiment: Observations for Boundary Layer and Troposphere (grant no. GYHY201406001), the National Natural Science Foundation of China (NSFC, grant no. 91337213, 41230419, and 41675041).

References

Anders, A.M., Roe, G.H., Hallet, B., Montgomery, D.R., Finnegan, N.J., Putkonen, J., 2006. Spatial Patterns of Precipitation And Topography in the Himalaya. Vol. 398. pp. 39–53.

Barros, A.P., Joshi, M., Putkonen, J., Burbank, D.W., 2000. A study of the 1999 monsoon rainfall in a mountainous region in central Nepal using TRMM products and rain gauge observations. Geophys. Res. Lett. 27, 3683–3686.

Beauchamp, R.M., Chandrasekar, V., Chen, H., Vega, M., 2015. Overview of the D3R observations during the IFloodS field experiment with emphasis on rainfall mapping and microphysics. J. Hydrometeorol. 16, 2118–2132.

Benn, D.I., Owen, L.A., 1998. The role of the Indian summer monsoon and the mid-latitude westerlies in Himalayan glaciation: review and speculative discussion. J. Geol. Soc. 155, 353–363.

Bhatt, B.C., Nakamura, K., 2005. Characteristics of monsoon rainfall around the Himalayas revealed by TRMM precipitation radar. Mon. Weather Rev. 133, 149–165.

Biggerstaff, M.I., Listemaa, S.A., 2000. An improved scheme for convective/stratiform echo classification using radar reflectivity. J. Appl. Meteorol. 39, 2129–2150.

Bookhagen, B., Burbank, D.W., 2006. Topography, relief, and TRMM-derived rainfall variations along the Himalaya. Geophys. Res. Lett. 33.

Boos, W.R., Kuang, Z., 2010. Dominant control of the South Asian monsoon by orographic insulation versus plateau heating. Nature 463 (218-U102).

Chen, Y.L., Fu, Y.F., 2017. Characteristics of VIRS signals within pixels of TRMM PR for warm rain in the tropics and subtropics. J. Appl. Meteorol. Climatol. 56, 789–801.

Chen, Y.L., Fu, Y.F., 2018. Tropical Echo-top height for precipitating clouds observed by multiple active instruments aboard satellites. Atmos. Res. 199, 54–61.

Chen, F., Fu, Y., Liu, P., Yang, Y., 2016. Seasonal variability of storm top altitudes in the tropics and subtropics observed by TRMM PR. Atmos. Res. 169, 113–126.

Chen, Y.L., Fu, Y.F., Xian, T., Pan, X., 2017. Characteristics of cloud cluster over the steep southern slopes of the Himalayas observed by CloudSat. Int. J. Climatol. 37, 4043–4052.

Dee, D.P., Uppala, S.M., Simmons, A.J., Berrisford, P., Poli, P., Kobayashi, S., Andrae, U., Balmaseda, M.A., Balsamo, G., Bauer, P., Bechtold, P., Beljaars, A.C.M., van de Berg, L., Bidlot, J., Bormann, N., Delsol, C., Dragani, R., Fuentes, M., Geer, A.J., Haimberger, L., Healy, S.B., Hersbach, H., Holm, E.V., Isaksen, L., Kallberg, P., Koehler, M., Matricardi, M., McNally, A.P., Monge-Sanz, B.M., Morcrette, J.J., Park, B.K., Peubey, C., de Rosnay, P., Tavolato, C., Thepaut, J.N., Vitart, F., 2011. The ERA-interim reanalysis: configuration and performance of the data assimilation system. Q. J. R. Meteorol. Soc. 137, 553–597.

Duan, A.M., Wu, G.X., 2005. Role of the Tibetan plateau thermal forcing in the summer climate patterns over subtropical Asia. Clim. Dyn. 24, 793–807.

Fu, Y.F., Liu, G.S., Wu, G.X., Yu, R.C., Xu, Y.P., Wang, Y., Li, R., Liu, Q., 2006. Tower mast of precipitation over the central Tibetan Plateau summer. Geophys. Res. Lett. 33.

Fu, Y., Pan, X., Xian, T., Liu, G., Zhong, L., Liu, Q., Li, R., Wang, Y., 2018. Precipitation characteristics over the steep slope of the Himalayas observed by TRMM PR and VIRS. Clim. Dyn. http://dx.doi.org/10.1007/s00382-017-3992-3.

Gadgil, S., Sajani, S., 1998. Monsoon precipitation in the AMIP runs. Clim. Dyn. 14, 659–689.

Hamada, A., Takayabu, Y.N., 2015. Improvements in detection of light precipitation with the global precipitation measurement dual-frequency precipitation radar (GPM DPR). J. Atmos. Ocean. Technol. 33, 653–667.

Hocking, L.M., 1959. The collision efficiency of small drops. Q. J. R. Meteorol. Soc. 85, 44–50.

Hou, A.Y., Kakar, R.K., Neeck, S., Azarbarzin, A.A., Kummerow, C.D., Kojima, M., Oki, R., Nakamura, K., Iguchi, T., 2014. The global precipitation measurement mission. Bull. Am. Meteorol. Soc. 95, 701 ± .

Houze, R.A., Wilton, D.C., Smull, B.F., 2007. Monsoon convection in the Himalayan region as seen by the TRMM precipitation radar. Q. J. R. Meteorol. Soc. 133, 1389–1411.

Hsu, H.H., Liu, X., 2003. Relationship between the Tibetan plateau heating and East Asian summer monsoon rainfall. Geophys. Res. Lett. 30.

Kotsuki, S., Terasaki, K., Miyoshi, T., 2014. GPM/DPR precipitation compared with a 3.5-km-resolution NICAM simulation. Sola 10, 204–209.

Kubota, T., Yoshida, N., Urita, S., Iguchi, T., Seto, S., Meneghini, R., Awaka, J., Hanado, H., Kida, S., Oki, R., 2014. Evaluation of precipitation estimates by at-launch codes of GPM/DPR algorithms using synthetic data from TRMM/PR observations. IEEE J. Select. Top. Appl. Earth Observat. Rem. Sens. 7, 3931–3944.

L'Ecuyer, T.S., Stephens, G.L., 2002. An estimation-based precipitation retrieval algorithm for attenuating radars. J. Appl. Meteorol. 41, 272–285.

Liu, C.T., Zipser, E.J., 2005. Global distribution of convection penetrating the tropical tropopause. J. Geophys. Res.-Atmos. 110.

Mason, B.J., 1972. Physics of thunderstorm. Proc. R. Soc. Lond. A Math. Phys. Sci. 327, 433.

Molnar, P., England, P., Martinod, J., 1993. Mantle dynamics, uplift of the Tibetan plateau, and the Indian monsoon. Rev. Geophys. 31, 357–396.

Murakami, T., 1987. In: Fein, J.S., Stephens, P.L. (Eds.), Orography and Monsoons. Chapter 12 in Monsoons. John Wiley and Sons, New York.

Nesbitt, S.W., Zipser, E.J., Cecil, D.J., 2000. A census of precipitation features in the tropics using TRMM: radar, ice scattering, and lightning observations. J. Clim. 13, 4087–4106.

Pang, H., Hou, S., Kaspari, S., Mayewski, P., Introne, D., Masson-Delmotte, V., Jouzel, J., Li, Z., He, Y., Hong, S., Qin, D., 2012. Atmospheric circulation change in the central Himalayas indicated by a high-resolution ice core deuterium excess record. Clim. Res. 53, 1–12.

Qie, X., Wu, X., Yuan, T., Bian, J., Lu, D., 2014. Comprehensive pattern of deep convective systems over the Tibetan plateau-south Asian monsoon region based on TRMM data. J. Clim. 27, 6612–6626.

Rasmussen, K.L., Houze, R.A., 2012. A flash-flooding storm at the steep edge of high terrain disaster in the Himalayas. Bull. Am. Meteorol. Soc. 93, 1713–1724.

Romatschke, U., Houze, R.A., 2011. Characteristics of precipitating convective systems in the South Asian monsoon. J. Hydrometeorol. 12, 3–26.

Romatschke, U., Medina, S., Houze, R.A., 2010. Regional, seasonal, and diurnal variations of extreme convection in the South Asian region. J. Clim. 23, 419–439.

Rose, C.R., Chandrasekar, V., 2006. A GPM dual-frequency retrieval algorithm: DSD profile-optimization method. J. Atmos. Ocean. Technol. 23, 1372–1383.

Shrestha, D., Singh, P., Nakamura, K., 2012. Spatiotemporal variation of rainfall over the central Himalayan region revealed by TRMM precipitation radar. J. Geophys. Res.-Atmos. 117.

Trenberth, K.E., Chen, S.C., 1988. Planetary-waves kinematically forced by Himalayan orography. J. Atmos. Sci. 45, 2934–2948.

Uppala, S., Dee, D., Kobayashi, S., Simmons, A.J., 2007. Evolution of reanalysis at ECMWF. In: Proceedings of Third WCRP International Conference on Reanalysis, (Jan 28–Feb 2, Tokyo, Japan).

Wang, Z., Duan, A., Wu, G., Yang, S., 2016. Mechanism for occurrence of precipitation over the southern slope of the Tibetan Plateau without local surface heating. Int. J. Climatol. 36, 4164–4171.

Wu, G., Liu, Y., Wang, T., Wan, R., Liu, X., Li, W., Wang, Z., Zhang, Q., Duan, A., Liang, X., 2007. The influence of mechanical and thermal forcing by the Tibetan plateau on Asian climate. J. Hydrometeorol. 8, 770–789.

Wu, G., Liu, Y., He, B., Bao, Q., Duan, A., Jin, F., 2012. Thermal controls on the Asian summer monsoon. Sci. Rep. 2.

Xian, T., Fu, Y., 2015. Characteristics of tropopause-penetrating convection determined by TRMM and COSMIC GPS radio occultation measurements. J. Geophys. Res.-Atmos. 120, 7006–7024.

Yanai, M.H., Li, C.F., Song, Z.S., 1992. Seasonal heating of the Tibetan plateau and its effects on the evolution of the Asian summer monsoon. J. Meteorol. Soc. Jpn. 70, 319–351.

Yang, K., Guo, X., He, J., Qin, J., Koike, T., 2011. On the climatology and trend of the atmospheric heat source over the Tibetan Plateau: an experiments-supported revisit. J. Clim. 24, 1525–1541.

Yuter, S.E., Houze, R.A., 1995. 3-dimensional kinematic and microphysical evolution of Florida cumulonimbus .2. frequency-distributions of vertical velocity, reflectivity, and differential reflectivity. Mon. Weather Rev. 123, 1941–1963.

Zwiebel, J., Van Baelen, J., Anquetin, S., Pointin, Y., Boudevillain, B., 2016. Impacts of orography and rain intensity on rainfall structure. The case of the HyMeX IOP7a event. Q. J. R. Meteorol. Soc. 1421, 310–319.